A $MoSe_2/WSe_2$ Heterojunction-Based Photodetector at Telecommunication Wavelengths

Hui Xue, Yadong Wang, Yunyun Dai, Wonjae Kim, Henri Jussila, Mei Qi, Jannatul Susoma, Zhaoyu Ren, Qing Dai, Jianlin Zhao, Kari Halonen, Harri Lipsanen, Xiaomu Wang, Xuetao Gan, and Zhipei Sun*

van der Waals (vdW) heterojunctions enable arbitrary combinations of different layered semiconductors with unique band structures, offering distinctive band engineering for photonic and optoelectronic devices with new functionalities and superior performance. Here, an interlayer photoresponse of a few-layer $MoSe_2/WSe_2$ vdW heterojunction is reported. With proper electrical gating and bias, the heterojunction exhibits high-sensitivity photodetection with the operation wavelength extended up to the telecommunication band (i.e. 1550 nm). The photoresponsivity and normalized photocurrent-to-dark current ratio reach up to 127 mA W^{-1} and 1.9×10^4 mW^{-1}, respectively. The results not only provide a promising solution to realize high-performance vdW telecommunication band photodetectors, but also pave the way for using sub-bandgap engineering of two-dimensional layered materials for photonic and optoelectronic applications.

1. Introduction

Photodetection at telecommunication wavelengths plays an important role in photonics and optoelectronics,[1] such as optical telecommunication,[2] sensing,[3] and imaging applications.[4] Nowadays, most of the commercial photodetectors are based on Ge and InGaAs, which possess obvious obstacles, such as low flexibility, miniaturization difficulty, and complex and expensive fabrication processes. Moreover, integrating Ge or III–V compound semiconductors with silicon substrates is a long-term technical challenge mainly due to the mismatched lattice constants and thermal expansion coefficients, which limit such devices in various demanding applications.[5] The creation of a van der Waals (vdW) heterojunction, formed by stacking different individual semiconducting transition-metal dichalcogenides (TMDs), offers a new dimension in making various high-performance electronic and optoelectronic devices.[6] For instance, TMDs are covalently bonded in-plane and held together out-of-plane by the vdW force, which are easily exfoliated and transferred to arbitrary substrates or stacked together to form heterojunctions regardless of lattice mismatch.[7] Among the various vdW heterostructures, type-II band alignment-based

H. Xue, Y. Wang, Dr. Y. Dai, Dr. H. Jussila, Dr. J. Susoma, Prof. K. Halonen, Prof. H. Lipsanen, Prof. Z. Sun
Department of Electronics and Nanoengineering
Aalto University
Espoo 02150, Finland
E-mail: hui.xue@aalto.fi

Y. Wang, Prof. X. Gan, Prof. J. Zhao
MOE Key Laboratory of Material Physics and Chemistry under Extraordinary Conditions, and Shaanxi Key Laboratory of Optical Information Technology
School of Science
Northwestern Polytechnical University
Xi'an 710072, China

Dr. W. Kim
VTT Technical Research Center of Finland
Espoo 02150, Finland

Dr. M. Qi
School of Information Science and Technology
Northwest University
Xi'an 710127, China

Prof. Z. Ren
Nanobiophotonic Center
State Key Lab Incubation Base of Photoelectric Technology and Functional Materials
International Cooperation Base of Photoelectric Technology and Functional Materials, and Institute of Photonics and Photon-Technology
Northwest University
Xi'an 710069, China

Prof. Q. Dai
Nanophotonics Research Division
CAS Center for Excellence in Nanoscience
National Center for Nanoscience and Technology
Beijing 100190, China

Prof. X. Wang
School of Electronic Science and Engineering
Nanjing University
Nanjing 210023, China

Prof. Z. Sun
QTF Centre of Excellence
Department of Applied Physics
Aalto University
FI-00076 Aalto, Finland

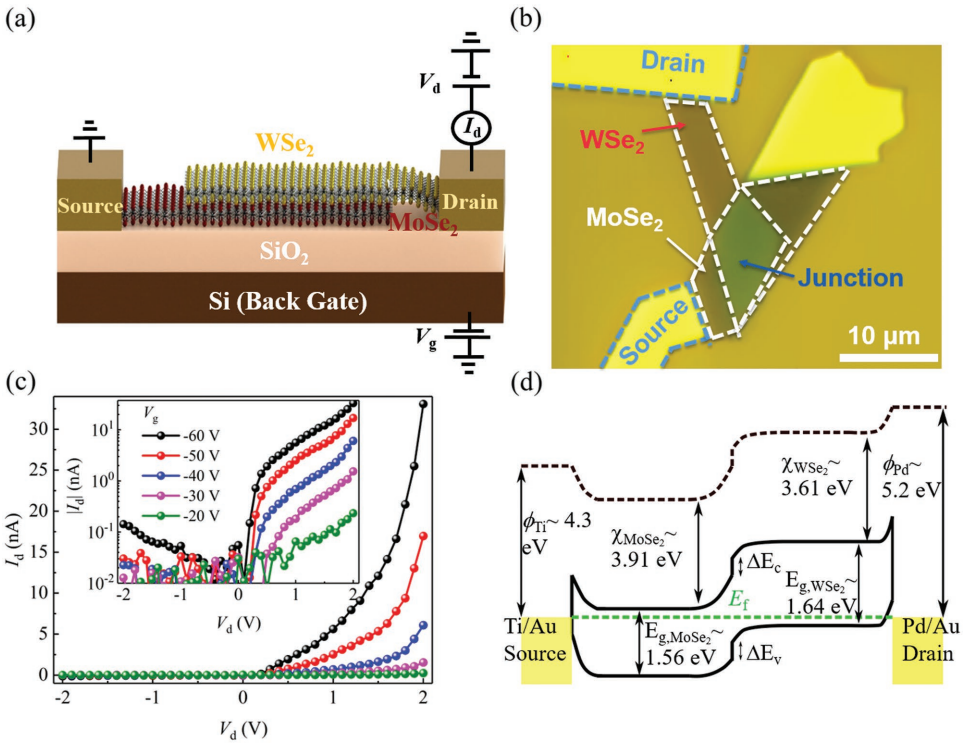

Figure 1. The $MoSe_2/WSe_2$ heterostructure device and its electrical properties. a) Schematic illustration of the heterojunction device together with the electrical connections used to characterize the device. b) Optical microscope image of the device. c) *I–V* characteristics measured with variable back-gate voltages in dark. Inset: *I–V* characteristics on the logarithmic scale. d) The schematic band diagrams of the device, where ϕ is the work function of metal; χ is the electron affinity of the flakes; E_f is the Fermi level, and E_g is the bandgap.

heterostructures allow the efficient separation of photon-excited electron–hole pairs, and thus improve the light to electrical signal conversion efficiency.[8] Recently, it has been proved that the type-II heterostructures can facilitate the interlayer transition of sub-bandgap photons for light detection at near-infrared (NIR) wavelengths.[9] However, thus far, the deomostrated TMDs heterostructure-based photodetectors suffer from a relatively small photoresponsivity (e.g., 40 nA W^{-1} at λ = 1550 nm in Zhang et al.[10]) possibly because of the high Schottky barrier at the contact regions and insufficient band bending in the overlapping regions. Therefore, TMD heterostructures-based photodetectors need to be further explored, in particular for the sub-bandgap photodetection at telecommunication bands.

Here, we demonstrate a high-sensitivity photodetector based on a few-layer $MoSe_2/WSe_2$ vdW heterojunction that exhibits a strong gate-dependent photoresponse. High photoresponsivity of 127 mA W^{-1} at λ = 1550 nm is achieved by applying a −70 V back gate voltage to decrease the Schottky barrier height at the metal-flake region and a −2 V reverse bias voltage to increase the band bending at the heterojunction region. The normalized photocurrent-to-dark current ratio (NPDR) of the device is $\approx 1.9 \times 10^4$ mW^{-1}. Further systematical investigation on the photoresponse to 1550 nm light reveals that tunneling-assisted transition is a key effect. Our work provides a new approach to extend the operation bandwidth of layered materials-based photodetectors for long-wavelength applications.

2. Results and Discussion

A schematic illustration and optical image of the demonstrated $MoSe_2/WSe_2$ heterostructure device are shown in **Figure 1**a,b, respectively. Few-layer $MoSe_2$ and WSe_2 flakes are mechanically exfoliated from their bulk materials, which are then transferred onto a 280 nm SiO_2/Silicon substrate.[11] An overlapping region is formed for the heterojunction by precisely controlling their locations. Ti/Au and Pd/Au (5 nm/50 nm and 5 nm/50 nm) metal electrodes are then patterned onto the $MoSe_2$ and WSe_2 flakes, respectively (Figure 1b). Here, different metal electrodes are chosen to facilitate the transport of charge carriers.[12] The thicknesses of the $MoSe_2$ and WSe_2 flakes, measured by atomic force microscopy, are ≈4 and ≈7 nm (Figure S1, Supporting Information), corresponding to ≈5- and ≈7-layer, respectively. Raman and photoluminescence spectroscopy is employed to confirm the high quality of our device after the fabrication processes (Figure S2a,b, Supporting Information).

The device is electrically characterized at room temperature by applying drain to source voltage (V_d) and back-gate voltage (V_g) in the configuration shown in Figure 1a. Note that, the 'forward' bias means applying a positive bias to the WSe_2 side, and the reverse bias means applying a negative bias to the WSe_2 side. The current–voltage curves (I_d–V_d) for the device (Figure 1c) exhibit typical feature as a field effect transistor with a p-type channel, clearly revealing that the current can only pass through the device when p-type WSe_2 is positively biased (forward bias,, i.e., $V_d > 0$ V).[13] Moreover, due to the ultrathin

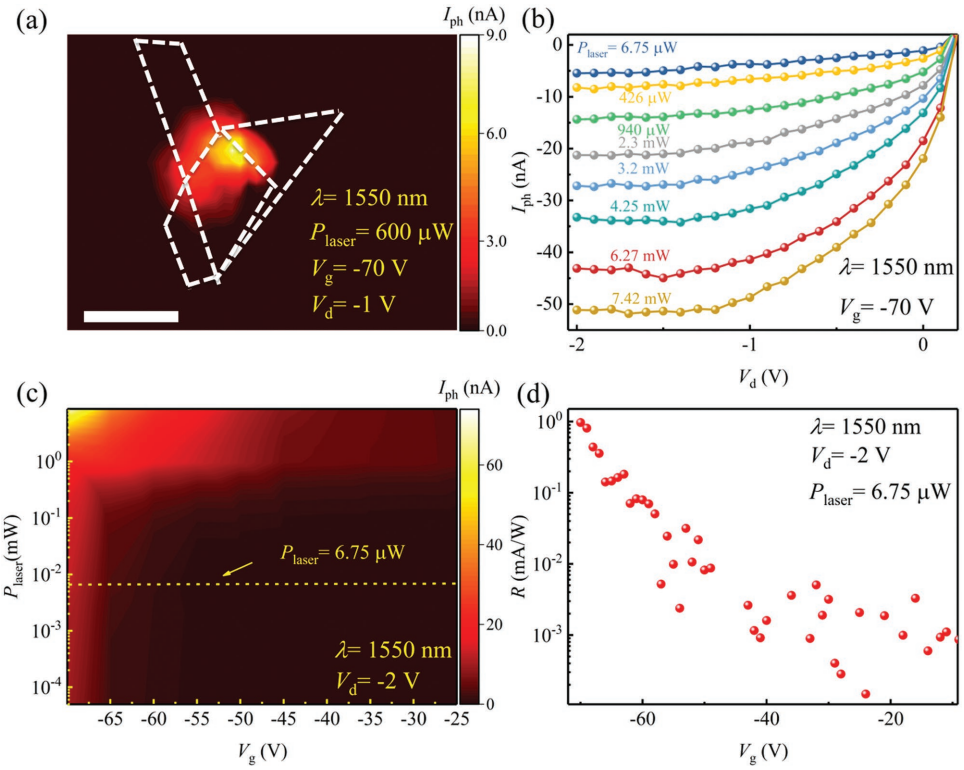

Figure 2. Photoresponse of the $MoSe_2/WSe_2$ heterojunction device at 1550 nm. a) Photocurrent mapping of the heterostructure. The white dotted regions represent the flakes in Figure 1b. b) I_{ph}–V_d of the $MoSe_2/WSe_2$ heterojunction. c) Photocurrent dependences on the V_g and P_{laser}. d) Responsivity dependence on the back-gate voltage. The scale bar is 10 μm.

nature of the heterostructure, the rectification ratio can be well tuned by the gate voltage, which increases as the gate voltage decreases. The rectification ratio of the device, defined as the ratio of forward and reverse current (I_d), reaches 10^4, indicating the formation of a *p-n* junction at the $MoSe_2/WSe_2$ interface. The asymmetry of I_d, obtained with forward and reversed bias when $V_g < 0$, indicates that the transport of carriers mainly depends on *p*-type WSe_2. To further understand the operation mechanisms of the device, a corresponding schematic band diagram is depicted in Figure 1d. Pristine metal contacts (i.e., Ti and Pd) and semiconductor layers (i.e., $MoSe_2$ and WSe_2) have different Fermi levels. Once in contact, according to Anderson's rule,[14] the ideal band formed in our heterostructure device consists of two Schottky junctions and one type-II heterojunction. The bottom of conduction band and the top of the valence band of WSe_2 ($MoSe_2$) are 3.61 eV (3.91 eV) and 5.25 eV (5.47 eV) and thus the offsets of the conduction band (ΔE_c) and valence band (ΔE_v) are about ≈0.3 and 0.22 eV, respectively.[12a,15]

To study the photoresponse characteristics of the device, scanning photocurrent measurements ($I_{ph} = I_d - I_{dark}$, where I_{dark} is the source current measured in dark) are carried out with a confocal optical microscope (Objective 100X, NA = 0.75). The spatially resolved photocurrent mapping with a λ = 1550 nm laser ($V_d = -1$ V, $V_g = -70$ V, and P_{laser} = 600 μW) reveals pronounced photocurrent generation in the overlapped region (**Figure 2**a). Importantly, photocurrent is negligible (<100 pA) when the device is forward biased even at high laser power, because of the decreased band bending induced by the forward bias (see discussion below). Note that the inhomogeneous photoresponse in the heterostructure region can be attributed to the non-uniform contacts between the $MoSe_2$ and WSe_2 flakes.[16] All the following measurements are carried out by locating the laser spot at the position where the largest photocurrent is generated. We then measure the I_d–V_d characteristics of the device at various P_{laser}, ranging from 6.75 μW to 7.42 mW, with a fixed gate voltage ($V_g = -70$ V), shown in Figure 2b. The obvious I_{sc} and V_{oc} can be seen from Figure 2b. This possibly indicates that apart from photoconductive effect, photovoltaic effect also contributes to the photocurrent generation.[17] The magnitude of the generated photocurrent strongly depends on V_d due to the increased carrier drift velocity, suggesting that higher photocurrent can be readily achieved by applying a larger drain to source voltage. The photocurrent as functions of the laser power and the gate voltage at $V_d = -2$ V is plotted in Figure 2c. It is clear that the magnitude of photocurrent decreases with the gate voltage and increases with the incident laser power. For example, when P_{laser} = 6.75 μW, the photocurrent is remarkable only when $V_g < -62$ V, revealing that larger band bending leads to a larger photocurrent.

To evaluate the performance of the photodetector, several figures of merits are calculated as follows. Responsivity (R) is typically calculated according to the equation $R = I_{ph}/P_{laser}$.[1b,18] Figure 2d shows the relationship between photoresponsivity and gate voltage at P_{laser} = 6.75 μW and $V_d = -2$ V. It is obvious that photoresponsivity decreases with V_g, indicating that higher

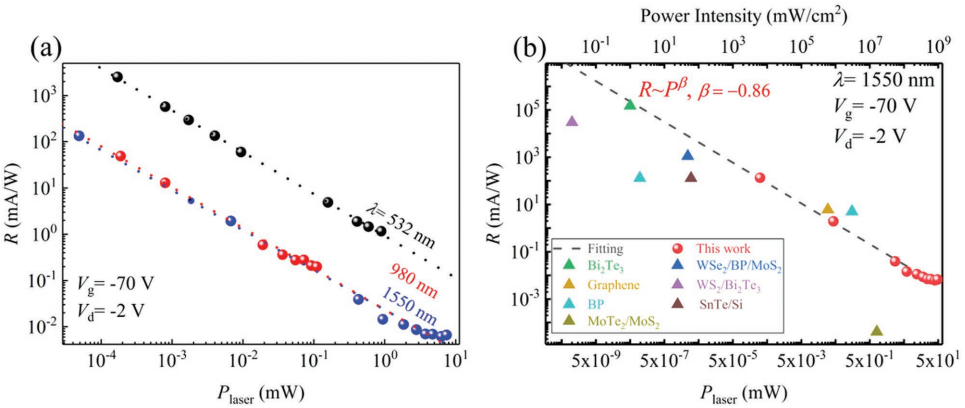

Figure 3. Photoresponsivity of the $MoSe_2/WSe_2$ heterojunction device. a) Summary of responsivity dependence of laser power at the wavelengths of 532, 980, and 1550 nm. b) Responsivity comparison of this work and typical published results (i.e., Bi_2Te_3,[22] Graphene,[23] WS_2/Bi_2Te_3,[24] $WSe_2/BP/MoS_2$,[25] SnTe/Si,[26] $MoTe_2/MoS_2$,[10] and BP[27]) at the wavelength of 1550 nm.

photoresponsivity can be readily achieved by applying a larger negative gate voltage.

We also measure the photoresponses at wavelengths of 532 and 980 nm for comparison (see Supporting Information). The response at the wavelength of 980 nm is similar to that at 1550 nm (see Figure S6, Supporting Information). This indicates that there is almost flat absorption at 980 and 1550 nm in multilayer WSe_2 and $MoSe_2$ flakes, which is confirmed by our absorption results (see Figure S3, Supporting Information). To compare the photoresponsivity at the same bias conditions under 532, 980, and 1550 nm laser excitations, the responsivity versus the laser powers are measured with the same bias and gating conditions, as shown in **Figure 3**a. It suggests that, the photoresponsivity decreases with the increased optical power for all three wavelengths, which might be caused by the saturation of electron–hole pair generation at higher incident laser powers and the increased surface recombination in the underlying SiO_2.[19] The maximum responsivity of our photodetector is 2 A W^{-1} at 532 nm (P_{laser} = 100 nW), 150 mA W^{-1} at 980 nm (P_{laser} = 50 nW), and 127 mA W^{-1} at 1550 nm (P_{laser} = 50 nW), when $V_g = -70$ V and $V_d = -2$ V. The responsivity at 532 nm is around 40 times higher than that at 1550 nm under the same incident laser power condition (according to the fit curves in Figure 3a). This can be attributed to higher absorption of the heterostructure at 532 nm than that at 1550 nm.

The *NPDR*, defined as NPDR = R/I_{dark}, is an important parameter that characterizes photodetector performance. The maximum NPDR is $\approx 2 \times 10^9$ mW^{-1} at 532 nm, 2.5×10^4 mW^{-1} at 980 nm and 1.9×10^4 mW^{-1} at 1550 nm, respectively, which could be attributed to no current flow through the device under reverse bias (Figure 1c). These high values of NPDR suggest that our device will be less limited by dark current shot noise, and potentially offers higher sensitivity.[20] By fitting the results in Figure 3b with the equation of $R \approx P^{\beta}$, the term β is obtained as −0.9 for 532 nm, −0.88 for 980 nm, and −0.86 for 1550 nm. This non-linear relationship is similar to the results reported with other IR photoconductors.[21] The deviation of β from 1 indicates the loss of photon-excited carriers, possibly due to the defects at the interface of the heterojunction. We also compare the responsivity of our device with previously published 2D material based photodetectors at λ = 1550 nm in Figure 3b (the comparison of photodetection at λ = 532 nm is shown in Figure S5, Supporting Information). Note that, the size of the heterojunction is around 80 μm^2; the spot size (S) of the 532 nm light on our device is 0.59 μm^2, and that of the 1550 nm light on our device is 4.9 μm^2. The performance of our sub-bandgap photodetector is comparable with the devices constituted by narrow bandgap materials (e.g., black phosphorus (BP) and Bi_2Te_3 working at the telecommunication bands), and also shows promising performance in the visible spectral region.

To rule out the other photocurrent generation mechanisms, such as photothermoelectric effect, I_{ph} (measured at $V_d = -2$ V, $V_g = -70$ V, and P_{laser} = 1 mW) as a function of time under modulated light excitation is depicted in Figure S7 (Supporting Information). It is obvious that the photoresponse to the 1550 nm light shows a stable and repeatable photocurrent, yielding an I_{on}/I_{off} of 100. To specify the mechanisms of our device, the schematic band diagrams and photocurrent mapping at λ = 532 nm of the heterostructure are plotted. **Figure 4**a–c depicts the band diagram at zero, revers, and forward biases, and Figure 4d–f shows the corresponding photocurrent mapping results at λ = 532 nm. When there is no bias (i.e., $V_d = V_g = 0$ V) and an external light excitation is applied (e.g., 532 nm light), electron–hole pairs are generated (Figure 4a). At the heterojunction region, with the effect of the built-in electric field, the photon-excited electrons move toward $MoSe_2$ and holes move toward WSe_2 separately, resulting in positive V_{oc} and negative I_{sc} (inset of Figure S4b in the Supporting Information). Corresponding spatial mapping of the photocurrent at this condition, as shown in Figure 4d, suggests the heterojunction produces its maximum photocurrent. To the contrary, there is negligible photocurrent in the metal-flake contacting regions due to the relatively low built-in electric field at this region. Note that the photocurrent mapping results only indicate the region where the dominate photocurrent is generated. Small photocurrent (e.g., ≈700 pA in Figure 4d) can also be observed in other parts of the device.

However, when the device is reverse biased ($V_d = -1$ V) at $V_g = -70$ V, the photo-generated electrons move to the $MoSe_2$ region and holes move to the WSe_2 region (Figure 4b). Moreover, the Schottky diode of the source contact is forward biased and the direction of the built-in electric field is the same as that of the external field. As a consequence, large photocurrent

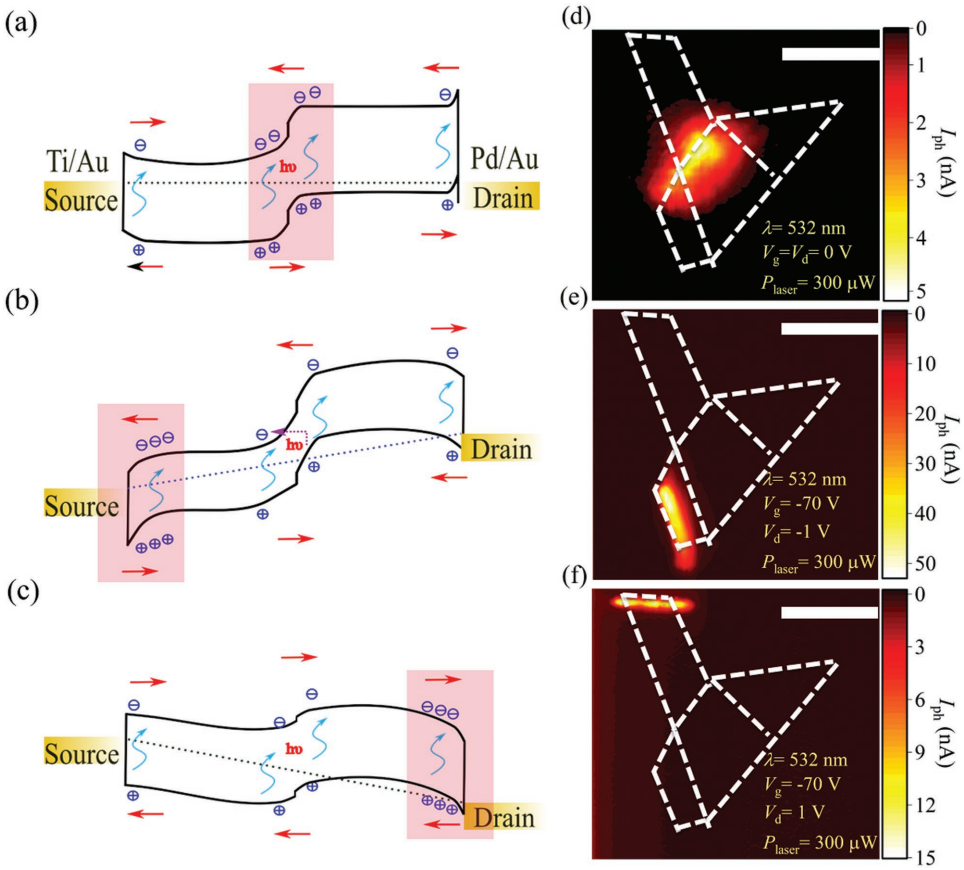

Figure 4. Operation principle of our heterojunction device. a–c) Band diagram of heterojunction and Schottky junctions, where (a) $V_g = V_d = 0$ V, (b) $V_g = -70$ V and $V_d = -1$ V and (c) $V_g = -70$ V and $V_d = 1$ V. The red arrows indicate the carrier movement direction. The blue arrows indicate the electron–hole pairs separation process. The pink rectangle regions indicate the position of the strongest built-in electric field. d–f) Photocurrent mapping of the heterojunction under different bias conditions. The dashed lines outline the flakes and heterojunction.

appears near the source contact (Figure 4e). While the device is forward biased with a large negative gate voltage (e.g., V_d = 1 V and V_g = –70 V), the photo-generated electrons move to the WSe_2 region and holes move to the $MoSe_2$ region (Figure 4c). Also, at the drain contact, the direction of the built-in electric field is the same as that of the external field. Therefore, when the light is incident on this region, photon-excited carriers will be dissociated more efficiently, resulting in the photocurrent enhancement near the drain electrode (Figure 4f).

Therefore, the gate-tunable photodetection at telecommunication wavelength can be explained utilizing these band bending mechanisms. The device shows high response to 1550 nm light, though the bandgap alignment of the two individual flakes and the calculated interlayer bandgap of the heterostructure is far beyond 0.8 eV. With a properly gating and biasing condition, the band bending at the heterojunction interface can be increased. This increased bending can potentially transfer the photon-excited electrons, with energy lower than that of the intrinsic bandgap of WSe_2, to the conduction band of $MoSe_2$. In our device, a built-in electric field, back-gate voltage, together with a reverse bias, contribute to a high electrostatic field, leading to the edges of conduction band and valence band being tilted along the direction of the electric field, and thus the wave functions have a tail extending into the bandgap region. Since the absorption coefficient is proportional to the magnitude square of the overlap integral of the *e–h* wave functions, the tunneling tails significantly enhance the *e–h* interactions with sub-bandgap photons,[28] contributing to the tunneling-assisted transition in the band-bending heterojunction area.[29] In our device, when a 10^5–10^6 V cm^{-1} electrical field is applied together with the high built-in electric field, the tunneling-assisted transition occurs, resulting in the sub-band response.[29a] Zhang et al.[30] have reported that the orientations of individual layers in the heterojunctions can affect their photodetection performance. We randomly stack a few WSe_2 and $MoSe_2$ heterostructure devices, which show similar photoresponses. This indicates that the flake orientations in the heterojunction do not affect the photoresponse of our heterostructures. Nevertheless, we think that the relationship between the flake orientations in the heterojunction and the photoresponse deserve further investigation.

3. Conclusion

In summary, we report a few-layer $MoSe_2/WSe_2$ heterojunction-based sub-bandgap photodetector. By controlling the electrostatic gating, the device shows high photodetection performance

at telecommunication wavelengths, with a maximum photoresponsivity of 127 mA W^{-1} and an NPDR of 1.9×10^4 mW^{-1}. Such a high performance can be attributed to the tunneling-assisted transition by properly gating and biasing the device. Our novel heterojunction photodetector shows an attractive platform for practical applications of utilizing few-layer TMDs-based heterojunctions, as well as paving a new way for novel, high-performance optoelectronics devices.

4. Experimental Section

Few-layer $MoSe_2$ was first mechanically exfoliated from the bulk material, which was then transferred onto a 280 nm SiO_2/Silicon substrate. The few-layer WSe_2 was then exfoliated and transferred onto the $MoSe_2$ to achieve the vdW heterojunction. The standard e-beam lithography process was used to define drain electrode on WSe_2 part. Pd/Au (5 nm/50 nm) was then be evaporated as metal contacts followed by a liftoff process. Another e-beam lithography process was repeated to define source electrode on the $MoSe_2$ part. Ti/Au (5 nm/50 nm) is then be evaporated as metal contacts followed by a liftoff process. The electric measurements were performed using to Keithley 2400 sourcemeters. All the electrical and optical measurements were performed in the ambient atmosphere.

Supporting Information

Supporting Information is available from the Wiley Online Library or from the author.

Acknowledgements

H. Xue and Y. Wang contributed equally to this work. Luke Baker helped with the manuscript revision. This research was supported by the Academy of Finland (276376, 284548, 295777, 304666, 312297, 312551, and 314810); TEKES (OPEC); the European Union's Seventh Framework Program (No. 631610); China Scholarship Council; the International Science and Technology Cooperation Project of China (No. 2014DFR10780). The authors also acknowledge the provision of technical facilities of the Micronova, Nanofabrication Centre of Aalto University.

Conflict of Interest

The authors declare no conflict of interest.

Keywords

$MoSe_2$, photodetectors, sub-bandgap photodetection, van der Waals heterojunction, WSe_2

[1] a) A. M. Gobin, M. H. Lee, N. J. Halas, W. D. James, R. A. Drezek, J. L. West, *Nano Lett.* **2007**, *7*, 1929; b) G. Konstantatos, E. H. Sargent, *Nat. Nanotechnol.* **2010**, *5*, 391; c) G. Hu, T. Albrow-Owen, X. Jin, A. Ali, Y. Hu, R. C. T. Howe, K. Shehzad, Z. Yang, X. Zhu, R. I. Woodward, T. C. Wu, H. Jussila, J. B. Wu, P. Peng, P. H. Tan, Z. Sun, E. J. R. Kelleher, M. Zhang, Y. Xu, T. Hasan, *Nat. Commun.* **2017**, *8*, 278.

[2] S. J. Su, B. W. Cheng, C. L. Xue, W. Wang, Q. A. Cao, H. Y. Xue, W. X. Hu, G. Z. Zhang, Y. H. Zuo, Q. M. Wang, *Opt. Express* **2011**, *19*, 6408.

[3] B. Nabet, A. Cola, A. Cataldo, X. Chen, F. Quaranta, *P. Soc. Photo.-Opt. Ins.* **2002**, *51*, 2063.

[4] C. B. Les, *Photonics Spectra.* **2009**, *43*, 27.

[5] Y. B. Bolkhovityanov, O. P. Pchelyakov, *Phys.-Uspekhi* **2008**, *51*, 437.

[6] a) R. Cheng, D. Li, H. Zhou, C. Wang, A. Yin, S. Jiang, Y. Liu, Y. Chen, Y. Huang, X. Duan, *Nano Lett.* **2014**, *14*, 5590; b) M. H. Chiu, C. Zhang, H. W. Shiu, C. P. Chuu, C. H. Chen, C. Y. Chang, C. H. Chen, M. Y. Chou, C. K. Shih, L. J. Li, *Nat. Commun.* **2015**, *6*, 7666; c) C. Huang, S. Wu, A. M. Sanchez, J. J. Peters, R. Beanland, J. S. Ross, P. Rivera, W. Yao, D. H. Cobden, X. Xu, *Nat. Mater.* **2014**, *13*, 1096; d) P. Rivera, J. R. Schaibley, A. M. Jones, J. S. Ross, S. Wu, G. Aivazian, P. Klement, K. Seyler, G. Clark, N. J. Ghimire, J. Yan, D. G. Mandrus, W. Yao, X. Xu, *Nat. Commun.* **2015**, *6*, 6242; e) S. Tongay, W. Fan, J. Kang, J. Park, U. Koldemir, J. Suh, D. S. Narang, K. Liu, J. Ji, J. Li, R. Sinclair, J. Wu, *Nano Lett.* **2014**, *14*, 3185; f) V. O. Ozcelik, J. G. Azadani, C. Yang, S. J. Koester, T. Low, *Phys. Rev. B* **2016**, *94*, 035125; g) A. Autere, H. Jussila, Y. Dai, Y. Wang, H. Lipsanen, Z. Sun, *Adv. Mater.* **2018**, *30*, 1705963; h) Z. P. Sun, A. Martinez, F. Wang, *Nat. Photonics* **2016**, *10*, 227; i) S. Yuan, C. Shen, B. Deng, X. Chen, Q. Guo, Y. Ma, A. Abbas, B. Liu, R. Haiges, C. Ott, T. Nilges, K. Watanabe, T. Taniguchi, O. Sinai, D. Naveh, C. Zhou, F. Xia, *Nano Lett.* **2018**, *18*, 3172; j) Y. Gao, R. J. Shiue, X. Gan, L. Li, C. Peng, I. Meric, L. Wang, A. Szep, D. Walker Jr., J. Hone, D. Englund, *Nano Lett.* **2015**, *15*, 2001; k) V. O. Ozcelik, M. Fathi, J. G. Azadani, T. Low, *Phys. Rev. Mater.* **2018**, *2*, 051003.

[7] A. K. Geim, I. V. Grigorieva, *Nature* **2013**, *499*, 419.

[8] F. Ceballos, M. Z. Bellus, H. Y. Chiu, H. Zhao, *ACS Nano* **2014**, *8*, 12717.

[9] a) K. Swaminathan, T. J. Grassman, L. M. Yang, Q. Gu, M. J. Mills, S. A. Ringel, *J. Appl. Phys.* **2011**, *110*, 063109; b) G. C. Wang, L. Li, W. H. Fan, R. Y. Wang, S. S. Zhou, J. T. Lue, L. Gan, T. Y. Zhai, *Adv. Funct. Mater.* **2018**, *28*, 1800339.

[10] K. Zhang, T. Zhang, G. Cheng, T. Li, S. Wang, W. Wei, X. Zhou, W. Yu, Y. Sun, P. Wang, D. Zhang, C. Zeng, X. Wang, W. Hu, H. J. Fan, G. Shen, X. Chen, X. Duan, K. Chang, N. Dai, *ACS Nano* **2016**, *10*, 3852.

[11] C. H. Lee, G. H. Lee, A. M. van der Zande, W. Chen, Y. Li, M. Han, X. Cui, G. Arefe, C. Nuckolls, T. F. Heinz, J. Guo, J. Hone, P. Kim, *Nat. Nanotechnol.* **2014**, *9*, 676.

[12] a) W. Zhang, M.-H. Chiu, C.-H. Chen, W. Chen, L.-J. Li, A. T. S. Wee, *ACS Nano* **2014**, *8*, 8653; b) A. Abderrahmane, P. J. Ko, T. V. Thu, S. Ishizawa, T. Takamura, A. Sandhu, *Nanotechnology* **2014**, *25*, 365202.

[13] N. Flöry, A. Jain, P. Bharadwaj, M. Parzefall, T. Taniguchi, K. Watanabe, L. Novotny, *Appl. Phys. Lett.* **2015**, *107*, 123106.

[14] R. L. Anderson, *IBM J. Res. Develop.* **1960**, *4*, 283.

[15] a) J. Kang, S. Tongay, J. Zhou, J. Li, J. Wu, *Appl. Phys. Lett.* **2013**, *102*, 012111; b) P. Tonndorf, R. Schmidt, P. Bottger, X. Zhang, J. Borner, A. Liebig, M. Albrecht, C. Kloc, O. Gordan, D. R. T. Zahn, S. M. de Vasconcellos, R. Bratschitsch, *Opt. Exp.* **2013**, *21*, 4908; c) S. Tongay, J. Zhou, C. Ataca, K. Lo, T. S. Matthews, J. B. Li, J. C. Grossman, J. Q. Wu, *Nano Lett.* **2012**, *12*, 5576.

[16] Y. Deng, Z. Luo, N. J. Conrad, H. Liu, Y. Gong, S. Najmaei, P. M. Ajayan, J. Lou, X. Xu, P. D. Ye, *ACS Nano* **2014**, *8*, 8292.

[17] M. M. Furchi, A. Pospischil, F. Libisch, J. Burgdorfer, T. Mueller, *Nano Lett.* **2014**, *14*, 4785.

[18] J. O. Island, S. I. Blanter, M. Buscema, H. S. van der Zant, A. Castellanos-Gomez, *Nano Lett.* **2015**, *15*, 7853.

[19] W. J. Yu, Y. Liu, H. Zhou, A. Yin, Z. Li, Y. Huang, X. Duan, *Nat. Nanotechnol.* **2013**, *8*, 952.
[20] X. M. Wang, Z. Z. Cheng, K. Xu, H. K. Tsang, J. B. Xu, *Nat. Photonics* **2013**, *7*, 888.
[21] Z. Sun, Z. Liu, J. Li, G. A. Tai, S. P. Lau, F. Yan, *Adv. Mater.* **2012**, *24*, 5878.
[22] A. Sharma, A. K. Srivastava, T. D. Senguttuvan, S. Husale, *Sci. Rep.* **2017**, *7*, 17911.
[23] T. Mueller, F. Xia, P. Avouris, *Nat. Photonics* **2010**, *4*, 297.
[24] J. Yao, Z. Zheng, G. Yang, *J. Mater. Chem. C* **2016**, *4*, 7831.
[25] H. Li, L. Ye, J. B. Xu, *ACS Photonics.* **2017**, *4*, 823.
[26] S. H. Gu, K. Ding, J. Pan, Z. B. Shao, J. Mao, X. J. Zhang, J. S. Jie, *J. Mater. Chem. A* **2017**, *5*, 11171.
[27] a) M. Engel, M. Steiner, P. Avouris, *Nano Lett.* **2014**, *14*, 6414; b) N. Youngblood, C. Chen, S. J. Koester, M. Li, *Nat. Photonics* **2015**, *9*, 247.
[28] Y. C. Zhou, Y. H. Liu, J. Cheng, Y. H. Lo, *Nano Lett.* **2012**, *12*, 5929.
[29] a) J. I. Pankove, *Optical Processes in Semiconductors*. Prentice-Hall, Englewood Cliffs, NJ, **1971**; b) W. Y. Wang, A. Klots, D. Prasai, Y. M. Yang, K. I. Bolotin, J. Valentine, *Nano Lett.* **2015**, *15*, 7440.
[30] a) J. Zhang, J. Wang, P. Chen, Y. Sun, S. Wu, Z. Jia, X. Lu, H. Yu, W. Chen, J. Zhu, G. Xie, R. Yang, D. Shi, X. Xu, J. Xiang, K. Liu, G. Zhang, *Adv. Mater.* **2016**, *28*, 1950; b) K. Wang, B. Huang, M. Tian, F. Ceballos, M. W. Lin, M. Mahjouri-Samani, A. Boulesbaa, A. A. Puretzky, C. M. Rouleau, M. Yoon, H. Zhao, K. Xiao, G. Duscher, D. B. Geohegan, *ACS Nano* **2016**, *10*, 6612.